One-pot synthesized boron-doped RhFe alloy with enhanced catalytic performance for hydrogen evolution reaction

Lishang Zhang[a,b,1], Jiajia Lu[a,1], Shibin Yin[a,*], Lin Luo[a], Shengyu Jing[b], Angeliki Brouzgou[e], Jianhua Chen[a], Pei Kang Shen[a], Panagiotis Tsiakaras[c,d,e,*]

[a] Guangxi Key Laboratory of Electrochemical Energy Materials, Collaborative Innovation Center of Renewable Energy Materials (CICREM), State Key Laboratory of Processing for Non-Ferrous Metal and Featured Materials, Guangxi University, Nanning 530004, China
[b] School of Information and Control Engineering, China University of Mining and Technology, Xuzhou 221116, Jiangsu, China
[c] Laboratory of Electrochemical Devices Based on Solid Oxide Proton Electrolytes, Institute of High Temperature Electrochemistry, RAS, Yekaterinburg 620990, Russia
[d] Laboratory of Materials and Devices for Electrochemical Power Industry, Ural Federal University, 19 Mira Str., Yekaterinburg 620002, Russia
[e] Laboratory of Alternative Energy Conversion Systems, Department of Mechanical Engineering, School of Engineering, University of Thessaly, Pedion Areos, 38834, Greece

ARTICLE INFO

ABSTRACT

Electrochemical water splitting has been highly recognized as a clean and sustainable method to produce hydrogen with high purity. An one-pot method to synthesize boron-doped RhFe alloy with excellent catalytic performance for hydrogen evolution is reported in the present work. Rhodium-Iron (RhFe) alloy nanoparticles, with diameter ranging from 1 to 5 nm, are distributed uniformly on the carbon support. The corresponding physicochemical and electrochemical results display that the sample of Rh:Fe = 2:1 post-treated at 200 °C (BRF21) shows the best performance for hydrogen evolution in 0.5 M H_2SO_4 aqueous solution; it exhibits good catalytic activity at a near zero onset potential. The required overpotential is found to be of about 25 mV at a current density of 10 mA cm^{-2}, which is 4 mV less than that of commercial Pt/C (29 mV); the Tafel slope is also comparable (32 mV dec^{-1}) with Pt/C (30 mV dec^{-1}). This work may provide a facile and environmentally-friendly method to prepare B-doped catalysts with high electrochemical hydrogen evolution efficiency.

1. Introduction

Hydrogen, as renewable, sustainable, and high combustion heat energy carrier, has been increasingly demanded as an alternative resource to replace the exhaustible fossil fuels. More than 90% of the hydrogen production is achieved industrially through methane steam reforming and coal gasification [1]. However, huge amounts of fuels will be consumed, and a big quantity of environmentally harmful and hazardous gases will be emitted through these methods [2]. Therefore, increasing attention has been attracted upon the water splitting, which is inherently a high-performance and environmental-friendly method to produce hydrogen and oxygen. The electrolysis of water involves two reactions: the hydrogen evolution reaction (HER) at cathode and the oxygen evolution reaction (OER) at the anode [3]. During the HER process, protons from the electrolyte are absorbed on the surface of cathode electrode, and then reduced to hydrogen, as the voltage applied to the electrode become higher than HER's overpotential. Therefore, a catalyst with small overpotential is significant for hydrogen evolution, which could reduce power consumption for water splitting.

As known, platinum-based materials are the most efficient catalysts for hydrogen evolution in acid electrolyte, but platinum's expensiveness and rareness restricts its broad application [4–6]. Up-to-date, only few examples of noble metal-based catalysts could exceed the HER activity in acid electrolyte as compared to commercial Pt/C catalysts. Therefore, it remains necessary to develop catalysts with high catalytic activity and good stability for hydrogen evolution. As a result, earth-abundant non-Pt catalysts, such as Fe- [7,8], Co- [9], Ni- [10], Cu- [11], Mo- [12,13], and W- [14] based materials, have been widely investigated. Nevertheless, in comparison with Pt, their catalytic performance is still far from satisfactory. Consequently, the search for catalysts with high activity and good stability for HER still remains a challenge.

It has been reported that hydrogen evolution proceeds *via* a similar pathway to that of the hydrogenation one (hydro-treating process); e.g., hydro-desulfurization, where the reversible adsorption/desorption of hydrogen on catalyst is critical for achieving fast kinetics [15]. Very recently, Pu *et al.* [16] proved that a hydrogenation catalyst may also be active for HER. They successfully used a hydro-desulfurization/hydro-deoxygenation catalyst RuP_2 as a catalyst for HER, which exhibited

---

* Corresponding authors.
  E-mail addresses: yinshibin@gxu.edu.cn (S. Yin), tsiak@uth.gr (P. Tsiakaras).
[1] These authors contributed equally.

remarkable performance.

On the other hand, many authors have reported rhodium has excellent properties including chemical inertness towards mineral acids, good catalytic activities for hydrogenation reactions [17,18] and ethanol oxidation [19]. Although Rh with small Gibbs free energy, which is positive for atomic hydrogen adsorption according to the Sabatier's principle [20], many non-noble metal based materials exhibited better catalytic activity than Rh/C catalysts. Zhu *et al.* [21] synthesized rhodium/silicon catalysts for HER. They found that: (i) the Rh/SiNW catalysts showed catalytic activity even higher than the 40 wt% Pt/C catalysts at more negatively potential than −160 mV; and (ii) the regeneration of hydroxyl poisoning by Rh contributes to the long-term stability of Rh/SiNW catalysts. Cheng et al. [22] prepared few noble metal-MoS$_2$ catalysts, they found that the Rh-MoS$_2$ catalysts exhibited the best HER activity among their prepared noble metal-MoS$_2$ materials. Yoon *et al.* [23] synthesized hollow Rh$_2$S$_3$ nanoprisms with high amount of catalytically active sites and structural robustness for HER. The above-mentioned results demonstrate that the Rh-based materials could be good candidates for HER. In 1990, Fukuoka et al. [24] already used Rh/Fe alloy for hydrogenation. Especially, Golvano-Escobal et al. [25] prepared RhFe alloy by the aid of electrodeposition, and proved the HER catalytic activity of Rh/Fe alloy. They found that the formation of a bimetallic surface may likely: i. give rise to modifications of the electronic properties of both Rh and Fe metals; ii. alter the average Rh-Rh metal bond and iii. show improved catalytic activity compared to their pure counterparts.

Furthermore, it is well known that an important strategy of improving HER catalytic activity of catalysts concerns with the introduction of heteroatom elements, such as nitrogen, phosphorus and boron [26]. The reason is that the introduction of heteroatoms might regulate the electronic arrangements of carbon skeleton, and consequently increase the corresponding catalytic activity for HER. Recent reports also proved that B-contained materials could be efficient for enhancing the catalytic activity for hydrogen evolution [27–29]. Zhang *et al.* [30] synthesized Co@BCN material for HER and they found that the neighboring of B with C atom could affect its (Carbon's) valence orbital energy levels, and thus leading to a reduced ΔG_H*.

Herein, a method for one-pot synthesis of B-doped RhFe alloys with enhanced catalytic performance for hydrogen evolution is reported. The as-prepared material is stable in acidic conditions, and exhibits well HER activity in 0.5 M H$_2$SO$_4$ electrolyte. Samples with different Rh to Fe ratios were synthesized and reduced at different temperatures. The corresponding physicochemical and electrochemical characterizations were investigated and thoroughly discussed. The results indicate that the as prepared B-doped RhFe alloy catalysts, as compared with the best proposed materials, possess high catalytic activity and display good stability for hydrogen evolution reaction. This work may provide a facile method to prepare B-doped catalysts with high efficiency for water splitting.

2. Experimental

2.1. Preparation

All samples were composed of 20 wt% of metal and 80 wt% of carbon. Typically, boron-doped RhFe alloy with Rh:Fe = 2:1 in molar ratio was prepared as follows: 2.0 ml rhodium(III) nitrate (Rh(NO$_3$)$_3$) aqueous solution (20.0 mg Rh/ml) was added into 150.0 ml deionized water, followed by 0.19 mmol iron(III) nitrate nona-hydrate (Fe (NO$_3$)$_3$·9H$_2$O) and 200.0 mg commercial XC-72 carbon powders. After ultrasonication and stirring for 30 min, 0.57 mmol potassium borohydride (KBH$_4$) was slowly added into the above solution. After stirring for 4 h, the material was collected by centrifugation, washed with deionized water and dried at 80 °C under vacuum for 10 h. Finally, the resulting powders were heated in a tube furnace at 200 °C under a flow of 5%H$_2$/Ar for 3 h with a heating rate of 5 °C min^{-1}. Other samples

with different Rh to Fe molar ratio were prepared following the same procedure. Samples with boron-doped Rh/Fe were denoted as BRFxy-T (for example, the sample with Rh:Fe = 2:1 post-treated at 200 °C was denoted as BRF21-200). The temperature is 200 °C if the T is not specified, and the sample was briefly denoted as BRFxy. Sample without Fe was denoted as B-Rh and sample without Rh was denoted as B-Fe. The B-doped XC-72 carbon, denoted as B–C, was prepared by the same method with the absence of metal salt; the sample of Rh:Fe = 2:1 in molar ratio without boron, denoted as RF21, was synthesized by the same method using 10 ml 80% N$_2$H$_4$·H$_2$O instead of potassium borohydride.

2.2. Characterization

X-ray powder diffraction (XRD) measurements were carried out using a SmartLab X-ray diffractometer (Rigaku Corp., Japan) equipped with Cu-Ka radiation (λ = 0.15406 nm) source. The data were collected at 40 kV and 30 mA with 2θ angular regions between 20° and 90°, with a scan rate of 5° min^{-1}. X-ray photoelectron spectroscopy (XPS) spectra were recorded on a spectrometer ESCALab 250Xi (ThermoFisher Scientific, USA) with an Al X-ray source operated at 150 W. Scanning transmission electron microscopy (STEM) and energy dispersive X-ray spectroscopy (EDX) investigation was performed using a Titan ETEM G^2 80–300 (FEI Co., USA) at an accelerating voltage of 200 kV, providing information of particle size distribution and the composition of the catalysts.

Electrochemical measurements were performed using a computer-controlled Pine (Pine, USA) electrochemical workstation in a thermo-statically-controlled standard three-electrode cell at 25 °C. A reversible hydrogen electrode (RHE) and graphite rod were used as reference and counter electrode, respectively. A glassy carbon disk (5.0 mm in diameter) coated by the catalysts films was used as working electrode. The catalysts films were prepared as follows: 5.0 mg catalyst was dispersed in 1.0 mL solution containing 20.0 μL of 5 wt% Nafion solution and 980.0 μL of ethanol. A homogeneous ink was obtained after ultra-sonication for about 40 min and 20.0 μL of the as-prepared slurry was dropped on the electrode by using a micropipette, and then dried in air; the calculated catalysts loading was ~0.51 mg cm^{-2}. The Pt/C catalyst (20 wt% Pt/C, Johnson Matthey), as reference material, was similarly prepared with 10.0 μL of slurry on electrode. After the initial stabilization, the linear sweep voltammetry (LSV) curves were recorded with a scan rate of 5 mV s^{-1} in 0.5 M H$_2$SO$_4$. For the electrochemical stability tests, the HER curves were recorded after sweeping 1000 cycles from 0 to –0.2 V in acidic solution, and the chronoamperometry curves were obtained by holding the potential at −50 mV in 0.5 M H$_2$SO$_4$ aqueous solution.

The Tafel slopes were fitted to Tafel equation (η = a + b log(j)); where η (mV) denotes the applied overpotential, j (mA cm^{-2}) is related to the current density, b (mV dec^{-1}) represents the Tafel slope. Exchange current density (j_0) was calculated by extrapolating the Tafel plots to X-axis according to Tafel equation, assuming η equal to zero. It should be noted that all current densities were normalized by geometric area, and all polarization curves were collected without *IR*-correction in this work.

3. Results and discussion

3.1. Physicochemical characterization

Fig. 1 shows the XRD patterns of the as-prepared samples. As displayed in Fig. 1a and c, the peaks located at 2θ of 41.1°, 47.8°, 69.9° and 84.4° are assigned to (111), (200), (220) and (311) planes of Rh (PDF No.#050685), and peaks located at 2θ of 29.8°, 42.7°, 62.0° and 78.2° are assigned to (100), (110), (200) and (211) planes of FeRh alloy (PDF No.#650986). Obviously, as shown in Fig. 1b and d, the (220) peaks of Rh are well fitted to a Gaussian line shape, so the position of the peaks
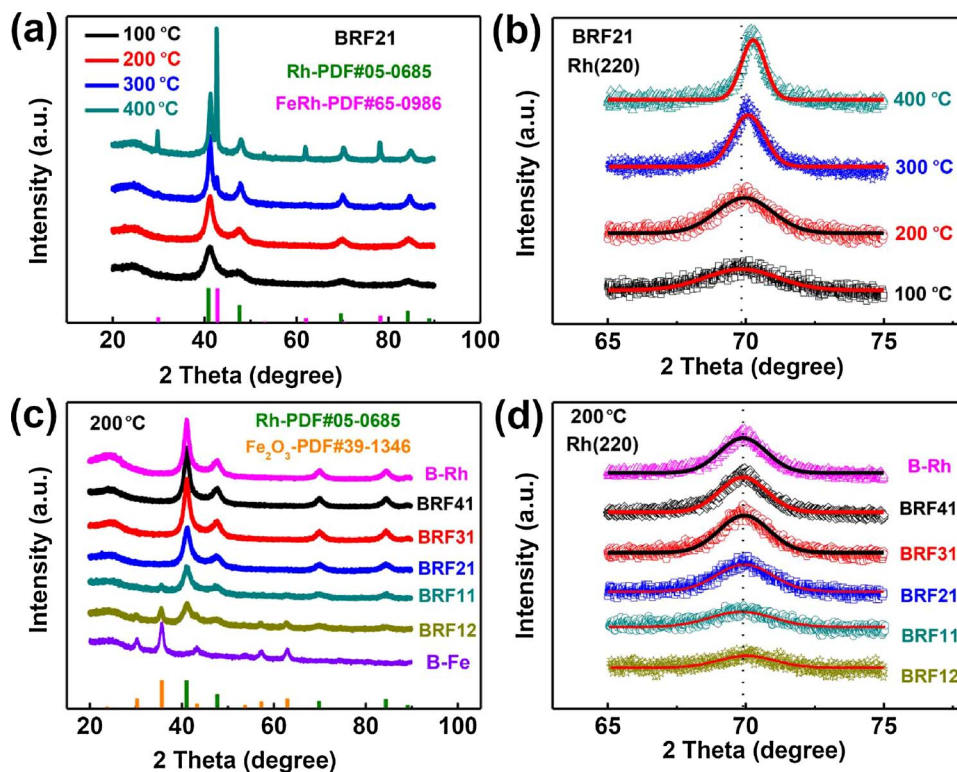
Fig. 1. (a) and (c) XRD curves of the as-prepared samples; (b) and (d) Curves fitting for (220) diffraction peaks in part (a) and (c).

maximum (θ_{max}) and full-width at half-maximum ($B_{2\theta}$) can be obtained with good precision.

The lattice parameters of Rh crystallites, α, were calculated from θ_{max} according to the Vegard's law [31]:

$$\alpha = \frac{\sqrt{2}\lambda_{k\alpha}}{\sin\theta_{max}} \tag{1}$$

where $\lambda_{k\alpha} = 0.154056$ nm. The lattice parameters of Rh crystallite in B-Rh, BRF41, BRF31, BRF21, BRF11 and BRF12, calculated from the (220) diffraction peak position, are 3.8032 Å, 3.8025 Å, 3.8011 Å, 3.8002 Å, 3.7984 Å and 3.7971 Å, respectively. The average crystal size, calculated using the full-width at half-maximum of the (220) diffraction and the Debye- Scherrer equation, are listed in Table 1.

Compared with B-Rh (3.8032 Å), the lattice parameters of BRF41, BRF31, BRF21, BRF11 and BRF12, are compressed by 0.0007 Å, 0.0021 Å, 0.003 Å, 0.0048 Å and 0.0061 Å, respectively. The differences of lattice parameters could be attributed to the incorporation of Fe atoms into Rh lattices formed a FeRh alloys, and different Fe contents could modify the surface states of the as-prepared RhFe alloy catalysts. Although it's difficult to find Fe peaks in patterns of BRF21-100 and 200, while as the temperature increases to 300 and 400 °C the intensity of FeRh peaks increases. This could be ascribed to the low crystallization of RhFe alloy at 100 and 200 °C. Furthermore, in Fig. 1c, BRF11 and BRF12 show Fe_2O_3 peaks, which are not evident in the other

samples. This may be due to the nature of Fe nanoparticles that near the surface of the as-prepared samples are easily oxidized in air.

X-ray photoelectron spectroscopy (XPS) was used to identify the surface status of the as-prepared catalysts. As shown in Fig. 2a, the results indicate that the surface of the samples of BRF21-100, BRF21-200, BRF21-300 and BRF21-400 are composed of Rh, Fe, C and O. Notably, in Fig. 2b, it is easy to find that the intensity of Fe2p peak decreases along with the increase of calcination temperature. This means that during the high temperature reduction Rh atoms move faster than Fe, because the different enthalpy of adsorption between Rh and Fe, and thus form a relatively Rh-rich surface, making the catalyst more stable in acidic conditions [32]. As shown in Table S1, the atomic percentage of Rh from XPS data increases with the rise of temperature. Furthermore, Fe and its oxides, which near the surface will inevitably dissolve in acid solution, may increase the electrochemical surface area and enhance the corresponding catalytic activity for HER.

The peaks of B1s on the right of Fig. 2b located at about (192.0 eV) can be attributed to the boron oxides. The intensity of B1s peaks get weaker with higher temperature reduction, as shown in Table S1, the atomic percentage of boron decreases from 10.62 to 8.39. This may be due to the migration of Rh [32], and therefore fewer B exists near the surface at higher temperatures. Peak deconvolution of Rh3d could verify the existence of Rh° (307.5 and 312.5 eV) and Rh^{3+} (309.1 and 314.4 eV). Peak deconvolution of Fe2p could prove the existence of Fe^{3+} (711.5 and 725.2 eV) and two satellite peaks (718.4 and 733.2 eV) [33].

Transmission electron microscopy (TEM) was employed to characterize the morphology of the as-prepared samples. As it can be distinguished in Fig. 3a and d, the unique morphology of BRF21 is clearly revealed. The Rh/Fe nanoparticles (average diameter ~ 3.75 ± 0.5 nm) are homogeneously loaded on the XC-72 carbon support in highly uniform size distribution (Fig. 3a inset). The structure of Rh/Fe nanoparticles is clearly showed in the high resolution TEM (HRTEM) images (Fig. 3b, c), and the primary crystal planes of (111) and (200) of Rh can be observed. Furthermore, the high-angle annular dark-field scanning transmission electron microscopy (HAADF-STEM)

Table 1
Structural parameters of the samples post-treated at 200 °C extracted from X-ray powder diffraction.

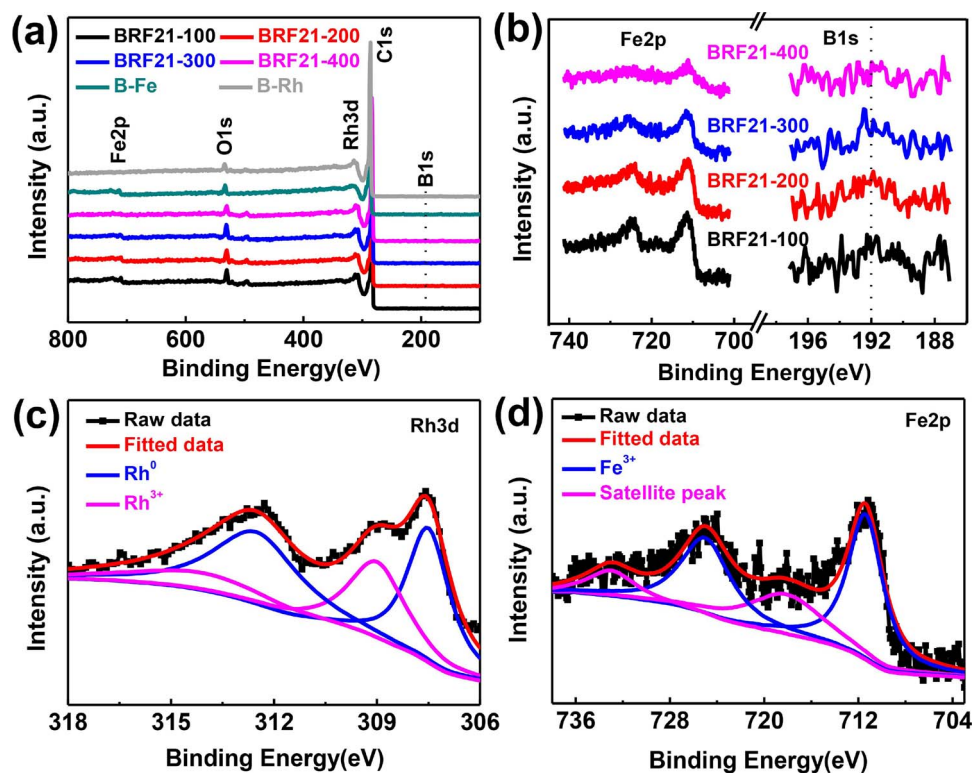| Catalyst	2θ (degree) (220) facet	Lattice parameter(Å) α	Crystal size (nm)
B-Rh	69.9021	3.8032	4.79
BRF41	69.9142	3.8025	4.62
BRF31	69.9427	3.8011	4.48
BRF21	69.9517	3.8002	4.01
BRF11	69.9908	3.7984	3.53
BRF12	70.0263	3.7971	4.01

Fig. 2. (a) XPS summary of BRF21-100(200, 300 and 400), B-Fe and B-Rh; (b) Fe2p and B1s of the as-prepared samples; (c) Rh3d and (d) Fe2p of BRF21.
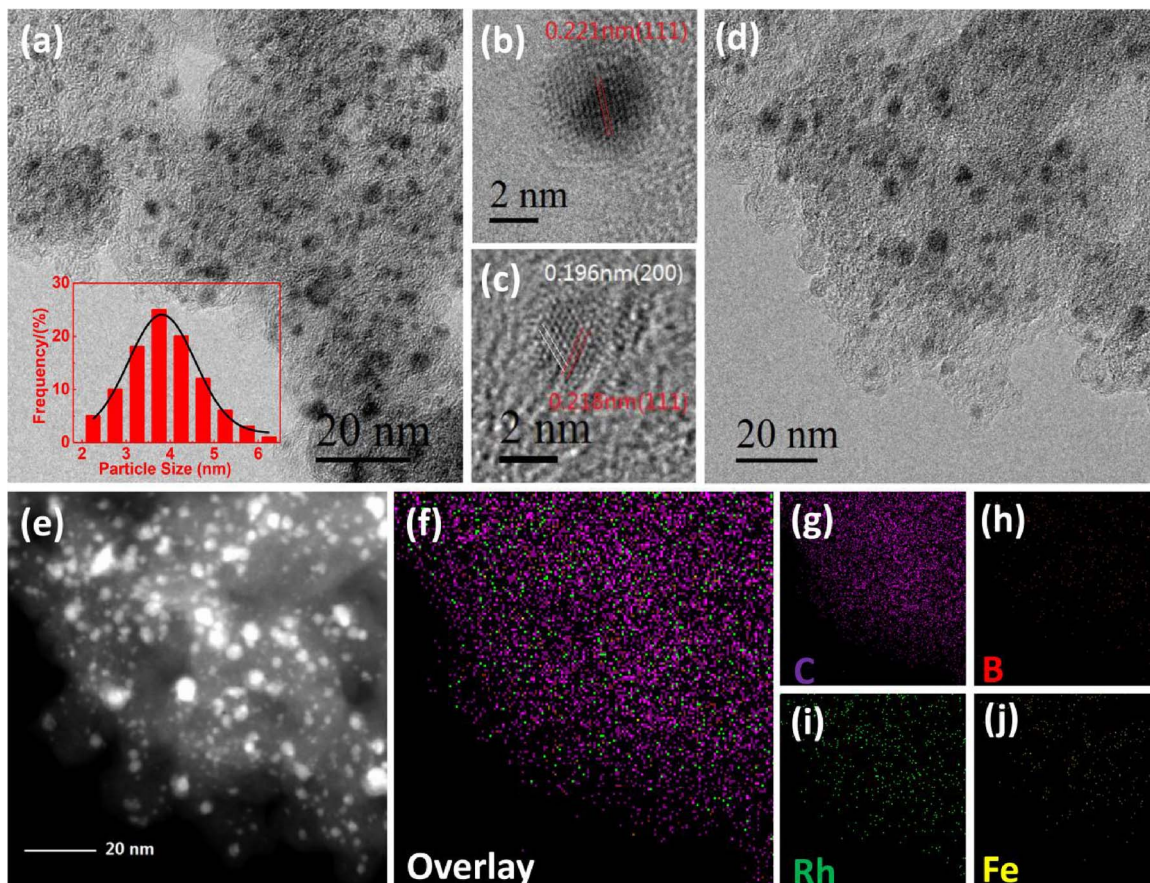

Fig. 3. (a) and (d) TEM, (b) and (c) HRTEM images of BRF21, (e) HAADF and (f)-(j) EDS mapping images of the corresponding area from (d).
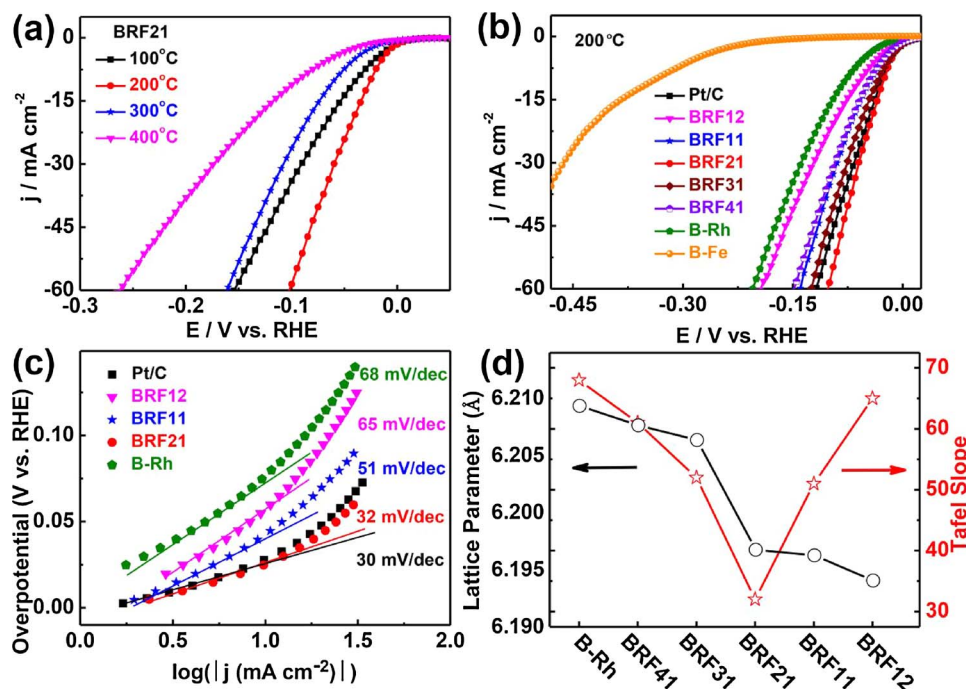
Fig. 4. Electrochemical measurements of the as-prepared samples for hydrogen evolution in 0.5 M H$_2$SO$_4$ aqueous solution. (a) Polarization curves of samples calcinated at different temperatures; (b) polarization curves of samples with different molar ratios post-treated at 200 °C; (c) the corresponding Tafel plots of (b); and (d) the plotting of lattice parameters and Tafel slopes in different samples.

(Fig. 3e) coupled with energy-dispersive X-ray (EDX) spectroscopy element mapping images (Fig. 3f–j) further indicate the homogeneous distribution of the Rh, Fe and B elements on the carbon support.
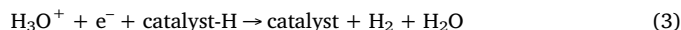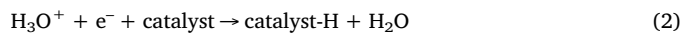
3.2. Electrochemical characterization

The as-prepared materials were evaluated for HER in 0.5 M H$_2$SO$_4$ aqueous solution with a scan rate of 5 mV s^{-1}. For comparison, the commercial 20 wt% Pt/C was also assessed. The relationship between calcination temperatures and HER activities were studied. As seen in Fig. 4a, among the four samples, the one calcinated at 200 °C exhibits the best catalytic activity for HER. Interesting, the catalytic activity rises when reduction temperature increases from 100 to 200 °C, and then falls at 300 and 400 °C. According to the XRD results, it is easy to find FeRh peaks in the samples treated at 300 and 400 °C, while there are negligible FeRh peaks in the samples treated at 100 and 200 °C. This means, as compared with well-crystallized FeRh alloys, the RhFe with relatively low alloy degree displays better catalytic activity for hydrogen evolution. The reason could be ascribed to the moderate adsorption/desorption energy for hydrogen evolution.

It should be noted that the samples with different Rh to Fe molar ratios that post-treated at 200 °C were further performed for HER. As displayed in Fig. 4b, the current density measured on BRF21 starts with a small onset potential which is better than that of Pt/C benchmark. The B-Rh sample shows inferior HER activity than boron-doped RhFe alloys and Pt/C, indicating that the synergistic effect between Rh and Fe could promote the HER activity. The reason may be that the lattice parameter of BRF21 was compressed by forming alloys, and the overlapping rate of neighboring atoms' electron orbitals is changed, which may modify the energy of electron transfer and increase the d-band density of electrons at Fermi level and improve the catalytic activity [34].
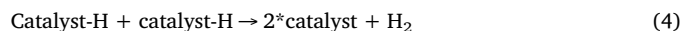
It is known that, the overpotential at a current density of 10 mA cm^{-2} is another important parameter for HER [35]. To achieve this current density, BRF21 demands overpotential value of only 25 mV while Pt/C needs 29 mV in this work. This value is apparently smaller than Pt/C and the values obtained from other samples. The cathodic current density increases rapidly with more negative potentials, which means that the as-prepared BRF21 possesses high catalytic activity and good Tafel slopes for HER. As can be seen from Fig. 4c, the fitted lines of

Tafel plots yield slope of *ca.* 32 mV dec^{-1} in 0.5 M H$_2$SO$_4$ aqueous solution for BRF21. This value is comparable to Pt/C of 30 mV dec^{-1} and smaller than other studied samples in this work.

The HER is a multi-step electrochemical process taking place on the surface of electrode that generates hydrogen. Generally, three possible steps are accepted in acidic solutions. In theory, the Tafel slope is 30 mV dec^{-1}, Heyrovský slope is 40 mV dec^{-1} and Volmer slope is 120 mV dec^{-1}. First is the Volmer step [36],

$$H_3O^+ + e^- + catalyst \rightarrow catalyst\text{-}H + H_2O \qquad (2)$$

$$H_3O^+ + e^- + catalyst\text{-}H \rightarrow catalyst + H_2 + H_2O \qquad (3)$$

or the Tafel step,

$$Catalyst\text{-}H + catalyst\text{-}H \rightarrow 2*catalyst + H_2 \qquad (4)$$

Tafel slope is an intrinsic property of catalysts, which is determined by the rate-limiting step of HER. The observed Tafel slope of 32 mV dec^{-1} for BRF21 (Fig. 4c) indicates that the primary discharge and electrochemical desorption may be the rate-limiting step, and the hydrogen evolution reaction on BRF21 mainly proceeds following the Volmer–Tafel mechanism. As displayed in Fig. 4d, BRF21 exhibits the smallest Tafel slope and a moderate lattice parameter among the prepared samples. The lattice parameter of BRF21 is 3.8002 Å; this value is smaller than that of B-Rh, BRF41 and BRF31 samples, while it is lager than that of BRF11 and BRF12. This further confirms that the appropriate Fe into Rh atoms may contribute to the high HER activity.

To further investigate the effect of boron dopants, the carbon support XC-72 and boron-doped XC-72, post-treated at 200 °C, were prepared and evaluated for HER. The XRD and XPS of B–C are shown in Figs S1 & S2. The (002) and (100) peaks of carbon could be easily found in XRD pattern. As seen in Fig. S2b, the peak of B1s at ~192 eV may indicate that the boron element is successfully doped in this sample. As shown in Fig. S4, the commercial carbon, denoted as C, possesses negligible catalytic activity for HER. While B–C exhibits relatively higher HER activity, which reaches 10 mA cm^{-2} at overpotential of about 408 mV. The Rh/Fe sample without boron dopant was also prepared. The XRD pattern of RF21 (Fig. S1b) could prove the existence of Rh (PDF No.#050685). Meanwhile, as displayed in XPS images (Fig. S3), no peak is located at ~192 eV in RF21, indicates there is no boron in the sample, only Rh3d and Fe2p peaks, demonstrate that this is an
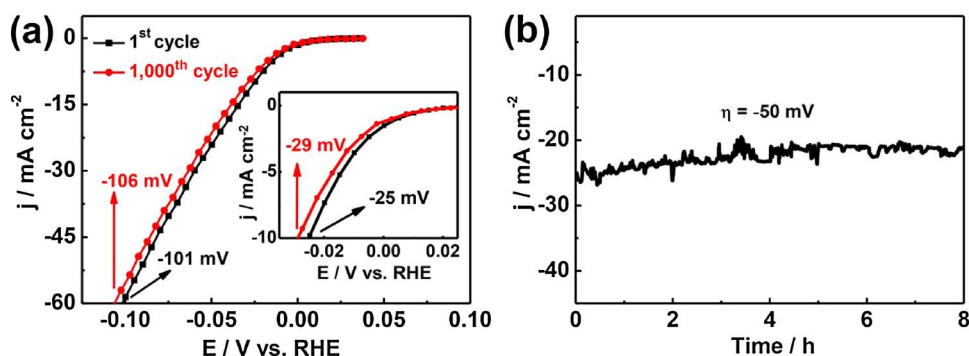
Fig. 5. (a) Polarization curves of BRF21 before and after 1000 cycles durability tests and the inset is the magnified curves of current density ranges from −10 to 1 mA cm−2; (b) chronoamperometry curves of the samples operated at $\eta = -50$ mV.

ideal sample that without boron. As displayed in Fig. S4, an impressive improvement can be observed, the BRF21 displays smaller overpotential than RF21, more than 70 mV is promoted at current density of 60 mA cm^{-2}. These results demonstrate the vital role of boron dopants for HER.

Long-term stability is another important parameter for the as-prepared catalysts. Herein, 1000 cycled-CV accelerated durability test and chronoamperometry curves were employed to assess the corresponding stability. As shown in Fig. 5a, after 1000 cycles' durability tests, the polarization curve of BRF21 negatively shifted about 4 mV at current density of 10 mA cm^{-2}.

From Fig. 5b, the chronoamperometry curve shows that the catalytic activity of BRF21 remains at about 84% after 8 h durability test at a potential of −50 mV. This demonstrates the excellent stability of BRF21 catalyst during HER process. After the stability test the BRF21 was characterized by XPS and the results are shown in Fig. S5. It can be distinguished that B1s and Rh3d own relatively smooth curves, while the Fe2p displays a disordered curve; this is a demonstration of Fe corrosion when surrounded by acid solutions. Moreover, in Table S2 the atomic percentage of Rh, Fe, B and O are listed; the atomic percentage of B rises from 9.57 to 12.51, before and after the durability test. Taking into account the corrosion of Fe, it is easier to understand that more B atoms were retained after the Fe and/or Rh atoms moved away. This could be an evidence of the fact that boron dopants may be stable in 0.5 M H$_2$SO$_4$ aqueous solution.

From the Tafel plots (Fig. S6a), the value of exchange current density (j_0) of BRF21, extrapolated according to Tafel equation from axis x, is found to be 1.91 mA cm^{-2}; even higher than that of commercial Pt/C (1.5 mA cm^{-2}) [37], indicating a superior intrinsic catalytic activity. In addition, the amount of hydrogen generated in the cathode compartment of the H-type electrolytic cell was collected by the water drainage method [16]. The amount of H$_2$ evolved at a constant current agrees with the theoretical value calculated for the same current (I), suggesting a Faradaic efficiency close ∼100% (Fig. S6b).

The small overpotential value (25 mV at 10 mA cm^{-2}), the small Tafel slope (32 mV dec^{-1}), the high exchange current density (1.91 mA cm^{-2}) and excellent stability in 0.5 M H$_2$SO$_4$ aqueous solution suggest that the BRF21 catalyst is among the highest catalytic activity as noble-metal materials in acid condition, as listed in Table 2, recently reported in literatures.

Such good catalytic performance for hydrogen evolution, obtained in this work over BRF21, could be ascribed to the following reasons:

(1) From Sabatier principle, Rh is inherently a good candidate with small Gibbs free energy for atomic hydrogen adsorption [45–47].
(2) The synergistic effect between Rh and Fe could further boost the HER activity. Specifically, the introduction of Fe could shorten the Rh-Rh distance, which could efficiently modify the electronic states of Rh, and alter the corresponding adsorption/desorption properties for H$^+$, and thus enhance the catalytic performance for hydrogen

Table 2
Comparison of HER activities in 0.5 M H$_2$SO$_4$ for BRF21 with literatures reported.

Catalyst	Overpotential at 10 mA cm^{-2} (mV)	Tafel slope (mV/dec)	Exchange current density (j_0/ mA cm^{-2})	Ref.
RuP$_2$@NPC	38	38	1.99	[16]
Rh$_2$S$_3$	117	44	/	[23]
Ru@C$_2$N	∼30	30	1.9	[37]
NiAu/Au	∼50	36	/	[38]
1D-RuO$_2$-CNx	93	40	0.22	[39]
Rh-Au-SiNW-2	62	24	0.0479	[40]
Rh$_2$P	20	/	/	[41]
Pt$_3$Ni$_2$NWs-S/C	∼25	/	/	[42]
Rh-Ag-Si	120	51	0.0871	[43]
Ru/C$_3$N$_4$/C	79	/	/	[44]
BRF21	25	32	1.91	This work

evolution [21].

(3) Boron is an electron deficient atom since it is surrounded by only six valence electrons, and thus, in order to form a stable octet, it co-ordinates with lone electron pairs of oxygen atom of water, hence increases the wetting properties by providing easy release of proton [48].
(4) Because the electronegativity for C (2.55) and for B (2.04), and B owns a homogeneous distribution, the 2p orbital of C may be first polarized by B, and then is able to donate extra electrons to the Rh/Fe nanoparticles. Consequentially a number of proton adsorption sites are generated [30].

4. Conclusions

In this work, a one-pot method for the synthesis of B-doped RhFe alloy with good catalytic performance for HER is developed. The as-prepared BRF21 catalyst is very robust under acidic condition. In 0.5 M H$_2$SO$_4$ aqueous solution, it shows very good HER activity and amazing stability, with a near zero onset overpotential. At a current density of 10 mA cm^{-2}, it needs an overpotential of about 25 mV, which is 4 mV less than that of commercial Pt/C (29 mV). Moreover, BRF21 shows a comparable Tafel slope of 32 mV dec^{-1} with Pt/C (30 mV dec^{-1}). Therefore, we can claim that boron-doping could be a helpful strategy for enhancing HER activity and this work could provide novel information for the preparation of highly efficient hydrogen evolution B-doped alloy catalysts.

Acknowledgements

Appendix A. Supplementary data

Supplementary material related to this article can be found, in the online version, at doi:https://doi.org/10.1016/j.apcatb.2018.02.034.

References

[1] X.X. Zou, Y. Zhang, Chem. Soc. Rev. 44 (2015) 5148–5180.
[2] J.J. Lu, L.S. Zhang, S.Y. Jing, L. Luo, S.B. Yin, Int. J. Hydrogen Energy 42 (2017) 5993–5999.
[3] G. Valenti, A. Boni, M. Melchionna, M. Cargnello, L. Nasi, G. Bertoni, R.J. Gorte, M. Marcaccio, S. Rapino, M. Bonchio, P. Fornasiero, M. Prato, F. Paolucci, Nat. Commun. 7 (2016) 13549.
[4] L. Ding, A. Wang, G. Li, Z. Liu, W. Zhao, C. Su, Y. Tong, J. Am. Chem. Soc. 134 (2012) 5730–5733.
[5] X. Du, S. Tan, P. Cai, W. Luo, G. Cheng, J. Mater. Chem. A 4 (2016) 14572–14576.
[6] M. Pang, C. Li, L. Ding, J. Zhang, D. Su, W. Li, C. Liang, Ind. Eng. Chem. Res. 175 (2010) 275–278.
[7] X. Long, G. Li, Z. Wang, H. Zhu, T. Zhang, S. Xiao, W. Guo, S. Yang, J. Am. Chem. Soc. 137 (2015) 11900–11903.
[8] A.M. Gómez–Marín, E.A. Ticianelli, Appl. Catal. B: Environ. 209 (2017) 600–610.
[9] M. Caban Acevedo, M.L. Stone, J.R. Schmidt, J.G. Thomas, Q. Ding, H.C. Chang, M.L. Tsai, J.H. He, S. Jin, Nat. Mater. 14 (2015) 1245–1251.
[10] A. Sivanantham, P. Ganesan, S. Shanmugam, Adv. Funct. Mater. 26 (2016) 4661–4672.
[11] J. Zhang, B. Xiao, X. Liu, P. Liu, P. Xi, W. Xiao, J. Ding, D. Gao, D. Xue, J. Mater. Chem. A 5 (2017) 17601–17608.
[12] Y. Jin, H. Wang, J. Li, X. Yue, Y. Han, P.K. Shen, Y. Cui, Adv. Mater. 28 (2016) 3785–3790.
[13] Z. Pu, S. Wei, Z. Chen, S. Mu, Appl. Catal. B: Environ. 196 (2016) 193–198.
[14] Y.J. Ko, J.M. Cho, I. Kim, D.S. Jeong, K.S. Lee, J.K. Park, Y.J. Baik, H.J. Choi, W.S. Lee, Appl. Catal. B: Environ. 203 (2016) 684–691.
[15] P. Xiao, W. Chen, X. Wang, Adv. Energy Mater. 5 (2015) 1500985.
[16] Z. Pu, I.S. Amiinu, Z. Kou, W. Li, S. Mu, Angew. Chem. Int. Ed. 56 (2017) 11559–11564.
[17] I. Nakamula, Y. Yamanoi, T. Imaoka, K. Yamamoto, H. Nishihara, Angew. Chem. Int. Ed. 50 (2011) 5830–5833.
[18] M.T. Reetz, G. Mehler, Angew. Chem. Int. Ed. 39 (2000) 3889–3890.
[19] P. Wang, S. Yin, Y. Wen, Z. Tian, N. Wang, J. Key, S. Wang, P.K. Shen, A.C.S. Appl. Mater. Interfaces 9 (2017) 9584–9591.
[20] Y. Liu, J. Wu, K.P. Hackenberg, J. Zhang, Y.M. Wang, Y. Yang, K. Keyshar, J. Gu, T. Ogitsu, R. Vajtai, J. Lou, P.M. Ajayan, B.C. Wood, B.I. Yakobson, Nat. Energy 2 (2017) 17127.
[21] L.L. Zhu, H.P. Lin, Y.Y. Li, L. Fan, Y. Lifshitz, M.Q. Sheng, S. Lee, M.W. Shao, Nat. Commun. 7 (2016) 12272–12279.
[22] Y. Cheng, S. Lu, F. Liao, L. Liu, Y. Li, M. Shao, Adv. Funct. Mater. 27 (2017) 1700359.
[23] D. Yoon, B. Seo, J. Lee, K.S. Nam, B. Kim, S. Park, H. Baik, S.H. Joo, K. Lee, Energy Environ. Sci. 9 (2016) 850–856.
[24] A. Fukuoka, T. Kimura, N. Kosugi, H. Kuroda, Y. Minai, Y. Sakai, T. Tominaga, M. Ichikawa, J. Catal. 126 (1990) 434–450.
[25] I. Golvano-Escobal, S. Surinach, M. Dolors Baro, S. Pane, J. Sort, E. Pellicer, Electrochim Acta 194 (2016) 263–275.
[26] G.F. Long, K. Wan, M.Y. Liu, Z.X. Liang, J.H. Piao, P. Tsiakaras, J. Catal. 348 (2017) 151–159.
[27] Y. Chen, G. Yu, W. Chen, Y. Liu, G.-D. Li, P. Zhu, Q. Tao, Q. Li, J. Liu, X. Shen, H. Li, X. Huang, D. Wang, T. Asefa, X. Zou, J. Am. Chem. Soc. 139 (2017) 12370–12373.
[28] J. Masa, P. Weide, D. Peeters, I. Sinev, W. Xia, Z. Sun, C. Somsen, M. Muhler, W. Schuhmann, Adv. Energy Mater. 6 (2016) 1502313.
[29] H. Park, A. Encinas, J.P. Scheifers, Y. Zhang, B.P.T. Fokwa, Angew. Chem. Int. Ed. 56 (2017) 5575–5578.
[30] H. Zhang, Z. Ma, J. Duan, H. Liu, G. Liu, T. Wang, K. Chang, M. Li, L. Shi, X. Meng, K. Wu, J. Ye, ACS Nano 10 (2016) 684–694.
[31] X. Ding, S. Yin, K. An, L. Luo, N. Shi, Y. Qiang, S. Pasupathi, B.G. Pollet, P.K. Shen, J. Mater. Chem. A 3 (2015) 4462–4469.
[32] D. Wang, H.L. Xin, R. Hovden, H. Wang, Y. Yu, D.A. Muller, F.J. Disalvo, H.D. Abruña, Nat. Mater. 12 (2013) 81–87.
[33] T. Yamashita, P. Hayes, Appl. Surf. Sci. 255 (2009) 8194.
[34] K.C. Poon, B. Khezri, Y. Li, R.D. Webster, H. Su, H. Sato, Chem. Commun. 52 (2016) 3556–3559.
[35] M.G. Walter, E.L. Warren, J.R. McKone, S.W. Boettcher, Q. Mi, E.A. Santori, N.S. Lewis, Chem. Rev. 110 (2010) 6446–6473.
[36] Z.W. Seh, J. Kibsgaard, C.F. Dickens, I.B. Chorkendorff, J.K. Norskov, T.F. Jaramillo, Science 355 (2017) 146–158.
[37] J. Mahmood, F. Li, S. Jung, M.S. Okyay, I. Ahmad, S. Kim, N. Park, H.Y. Jeong, J. Baek, Nat. Nanotechnol. 12 (2017) 441–446.
[38] H. Lv, Z. Xi, Z. Chen, S. Guo, Y. Yu, W. Zhu, Q. Li, X. Zhang, M. Pan, G. Lu, S. Mu, S. Sun, J. Am. Chem. Soc. 137 (2015) 5859–5862.
[39] T. Bhowmik, M.K. Kundu, S. Barman, ACS Appl. Mater. Interfaces 8 (2016) 28678–28688.
[40] B. Jiang, L. Yang, F. Liao, M. Sheng, H. Zhao, H. Lin, M. Shao, Nano Res. 10 (2017) 1749–1755.
[41] H. Duan, D. Li, Y. Tang, Y. He, S. Ji, R. Wang, H. Lv, P.P. Lopes, A.P. Paulikas, H. Li, S.X. Mao, C. Wang, N.M. Markovic, J. Li, V.R. Stamenkovic, Y. Li, J. Am. Chem. Soc. 139 (2017) 5494–5502.
[42] P. Wang, X. Zhang, J. Zhang, S. Wan, S. Guo, G. Lu, J. Yao, X. Huang, Nat. Commun. 8 (2017) 14580.
[43] B. Jiang, Y. Sun, F. Liao, W. Shen, H. Lin, H. Wang, M. Shao, J. Mater. Chem. A 5 (2017) 1623–1628.
[44] Y. Zheng, Y. Jiao, Y. Zhu, L.H. Li, Y. Han, Y. Chen, M. Jaroniec, S. Qiao, J. Am. Chem. Soc. 138 (2016) 16174–16181.
[45] T.F. Jaramillo, K.P. Jorgensen, J. Bonde, J.H. Nielsen, S. Horch, I. Chorkendorff, Science 317 (2007) 100–102.
[46] J. Greeley, M. Mavrikakis, Nat. Mater. 3 (2004) 810–815.
[47] J. Greeley, T.F. Jaramillo, J. Bonde, I.B. Chorkendorff, J.K. Norskov, Nat. Mater. 5 (2006) 909–913.
[48] M.A.R. Anjum, M.H. Lee, J.S. Lee, J. Mater. Chem. A 5 (2017) 13122–13129.